Instability of a liquid jet emerging from a droplet upon collision with a solid surface

H.-Y. Kim,[a)] Z. C. Feng,[b)] and J.-H. Chun
Department of Mechanical Engineering, Massachusetts Institute of Technology, Cambridge, Massachusetts 02139

A linear perturbation theory is developed to investigate the interface instabilities of a radially-expanding, liquid jet in cylindrical geometries. The theory is applied to rapidly spreading droplets upon collision with solid surfaces as the fundamental mechanism behind splashing. The analysis is based on the observation that the instability of the liquid sheet, i.e., the formation of the fingers at the spreading front, develops in the extremely early stages of droplet impact. The shape evolution of the interface in the very early stages of spreading is numerically simulated based on the axisymmetric solutions obtained by a theoretical model. The effects that factors such as the transient profile of an interface radius, the perturbation onset time, and the Weber number have on the analysis results are examined. This study shows that a large impact inertia, associated with a high Weber number, promotes interface instability, and prefers high wave number for maximum instability. The numbers of fingers at the spreading front of droplets predicted by the model agree well with those experimentally observed. © *2000 American Institute of Physics.*
[S1070-6631(00)00503-1]

I. INTRODUCTION

A droplet with large inertia frequently spreads with fingers extending from the edge when it impinges on a solid surface. Although the behavior of a spreading droplet after colliding with a target plane has been the subject of intense study for many years,[1–7] comparatively less work has been done on a splashing droplet. Levin and Hobbs[8] observed the formation of a crown, i.e., the detachment of a watersheet from a target surface, when a water drop impinges on a copper hemisphere. Stow and Hadfield[9] photographed the early development of a watersheet emerging from the drop/target contact area, and were able to distinguish splashing droplets from nonsplashing ones by the release of an unstable watersheet in the very early stages of spreading. Mundo *et al.*[10] characterized the size and velocity of the secondary droplets produced from a droplet colliding with a rotating disk at an angle. Thoroddsen and Sakakibara[11] were the first to perform a systematic study on the evolution of the fingers developing from a droplet interface spreading on a flat glass substrate. Furthermore, recent experiments[11,12] showed that the unstable azimuthal undulation is a characteristic feature of splashing. For this reason, we consider splashing to be the unstable expansion of the spreading front in colliding droplets, including crown formation as an extreme case of splashing. In this work, we study a fundamental mechanism which induces the instability of the spreading front, proposing it as an origin of splashing.

Significant experimental observations of splashing droplets are summarized as the following: (1) The instability is observed in the very early stages of spreading;[9,11] (2) splashing occurs when the impacting droplet has significant kinetic energy as compared to surface energy and it is promoted by rough target surfaces. A crown even develops under severe destabilizing conditions;[9,10] (3) increasing the impact inertia increases the number of fingers,[12] and this number slightly decreases during spreading.[11]

A few articles[10,11,13] have addressed the origin of splashing, although no conclusive theory has been developed. Allen[13] suggested that a radially decelerating interface of a spreading droplet be Rayleigh–Taylor unstable and calculated the wavelength of maximum instability based on the average deceleration required to bring the spreading to a halt. He modeled the radially extending flow into one-directional plane motion and assumed that the deceleration was due to viscous damping. However, his model overlooks the effects of changing interface length during spreading and the effect of curvature on the instabilities. In addition, the selection of the representative deceleration is somewhat arbitrary. Mundo *et al.*[10] suggested that the crown develops when the total energy of a droplet prior to impact exceeds the amount of energy dissipated by viscosity during spreading. On the other hand, Thoroddsen and Sakakibara[11] contended that the fingering is due to the Rayleigh–Taylor instability of the decelerating fluid ring at the droplet bottom before the droplet collides with a target.

In Fig. 1, we show rather interesting photographs of a splat formed by depositing a pure tin droplet on a 304 stainless steel surface polished using a diamond paste. The picture of the splat bottom [Fig. 1(b)] still exhibits the flow pattern during spreading owing to the fast freezing of the
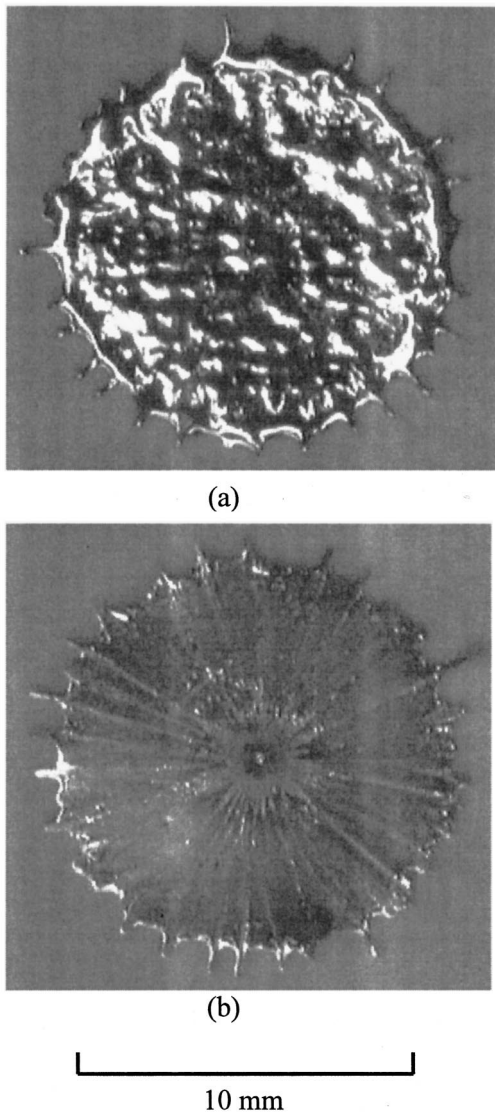
(a)

(b)

10 mm

FIG. 1. Splashed tin splat. (a) Top of the splat. (b) Bottom of the splat. The impact conditions: impact velocity=3.5 m/s, initial droplet diameter=2.6 mm, droplet temperature at impact=315 °C (freezing temperature of pure tin=232 °C), target temperature=30 °C, and We=203. The size and velocity of the droplet were measured using a high speed video system (Kodak Ektapro EM, Model 1012). Droplet temperature was calculated using the initial melt temperature and the flight distance.

molten metal droplet. It shows that fingers which developed at the splat edge in fact have their origins at the central area of the splat. A closer look at the figure reveals that the fingers have completely developed around the central area, with approximately half of the radius of the original droplet. It follows that those fingers have already formed before they start to be frozen, or before the spreading front radius reaches one half the length of the original droplet's radius. Consequently, this observation suggests that the formation mechanism of the fingers can only be understood by studying the behavior of the droplet right after the impact. The early stage of droplet impact is characterized by a rapid release of a liquid jet.[9,14,15] Therefore, we must study the early behavior of a liquid jet released upon impact to understand the mechanism of splashing. In this work, we propose the Rayleigh–

Taylor instability of the radially expanding sheet upon its generation, in cylindrical geometry, as a fundamental mechanism of splashing. Our study is similar to Allen's[13] in that both investigate the Rayleigh–Taylor instability of the spreading front. However, here we consider the changing interface length and curvature and suggest a different mechanism of liquid jet deceleration.

Although the Rayleigh–Taylor instability has been extensively studied for many years, most of the effort has been focused on the plane[16–19] and spherical geometries.[20–23] In particular, interests in cavitation bubbles, pulsations of underwater explosion bubbles, and sonoluminescence[24] have brought attention to the dynamics of spherical bubbles. The behavior of a gas bubble, in an incompressible liquid under adiabatic or isothermal conditions, is described by the Rayleigh–Plesset (RP) equation.[25,26] The distortion amplitude of the spherical interface is governed by an equation whose coefficients are time-dependent as ruled by the RP equation. When the amplitude of the radial oscillation is small, the governing equations for the shape modes are reduced to Mathieu's equation. On the other hand, Brenner *et al.*[27] examined both the Rayleigh–Taylor and the parametric instability mechanisms for a large amplitude case. In general, numerical methods are required to analyze such a case.

In the present work, we investigate the instabilities of a radially-expanding circular interface in cylindrical geometries. It is emphasized that our interest lies in studying the fundamental mechanism of the finger formation rather than the finger evolution which was intensively investigated by Thoroddsen and Sakakibara.[11] It is for this reason that we employ the potential theory in modeling the high speed flow in the very early stages of droplet impact. We do not extend our theory beyond the limit where the viscous effects become important, in which stage fingers already generated merely evolve. While the bubble dynamics are governed by the RP equation, the motion of the liquid sheet upon its release is ruled by the dynamics of the very early stages of droplet spreading. We first obtain a general equation governing the azimuthal instability of an expanding sheet by using domain perturbation methods and apply the results for the very initial stages of droplet impact. The dynamic conditions of a droplet prior to impact are represented by the Weber number in our analysis. Numerical simulation is employed to investigate the sensitivity of the instability analysis to the modeling assumptions and the role of impact conditions.

II. DERIVATION OF THE AMPLITUDE EQUATION

Consider a radially-expanding liquid jet whose expansion rate, i.e., radial velocity as a function of time, is known *a priori*. The stability of the edge of the two-dimensional, liquid jet subjected to an azimuthal disturbance is investigated. Without disturbance, its shape is given only by time, and its velocity is determined merely by time and radial distance. However, under the azimuthal disturbance, the location of the periphery is dependent upon an azimuthal angle, θ, as well as time, as shown in Fig. 2.

We nondimensionalize the flow parameters based on the characteristic radius R_D^* and the characteristic velocity U^*.
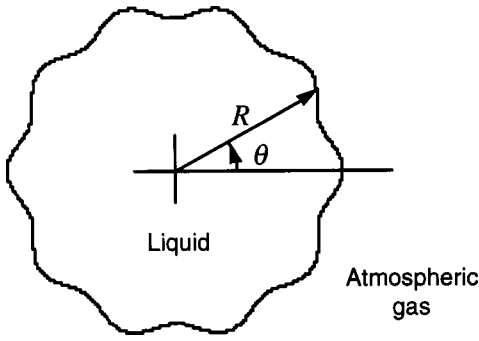
FIG. 2. Disturbed liquid sheet which expands radially.

In the case of liquid droplets, R_D^* and U^* correspond to the original droplet radius before impact and to the impact velocity, respectively. The characteristic time scale, τ^*, is given by $\tau^* = R_D^*/U^*$, and the velocity potential is scaled by $R_D^* U^*$. The following quantities are all nondimensionalized based on R_D^*, U^*, τ^*, and $R_D^* U^*$, and Appendix A shows their forms.

The velocity potential of the liquid, ϕ, is defined such that the radial velocity, v_r, and the azimuthal velocity, v_θ, satisfy, respectively,

$$v_r = \frac{\partial \phi}{\partial r}, \tag{1}$$

and

$$v_\theta = \frac{1}{r} \frac{\partial \phi}{\partial \theta}. \tag{2}$$

It is supposed that the velocity potential and the outer radius of the fluid R are slightly disturbed, so that they are expressed as

$$\phi = \phi_0(t,r) + \phi_1(t,r,\theta), \tag{3}$$

and

$$R = R_0(t) + R_1(t,\theta), \tag{4}$$

where ϕ_0 and R_0 denote the axisymmetric spreading solutions and ϕ_1 and R_1 are small perturbations. Due to the high Reynolds number associated with the high speed flow upon impact, we employ the governing equation for a potential flow:

$$\nabla^2 \phi = 0. \tag{5}$$

We model the axisymmetric liquid expansion by a line source at the center, giving the base flow solution as

$$\phi_0 = M(t) \ln r, \tag{6}$$

where M is the strength of the source. Then the base solution of the radial velocity is expressed as

$$\frac{\partial \phi_0}{\partial r} = \frac{M}{r}. \tag{7}$$

The kinematic boundary condition (KBC) at the edge of the expanding fluid is

$$\frac{\partial \phi}{\partial r} = \frac{\partial R}{\partial t} + \frac{1}{r^2} \frac{\partial \phi}{\partial \theta} \frac{\partial R}{\partial \theta}. \tag{8}$$

Using Eqs. (3) and (4), we rewrite KBC as

$$\frac{\partial \phi_0}{\partial r} + \frac{\partial \phi_1}{\partial r} = \frac{\partial R_0}{\partial t} + \frac{\partial R_1}{\partial t} + \frac{1}{r^2} \frac{\partial \phi_1}{\partial \theta} \frac{\partial R_1}{\partial \theta}. \tag{9}$$

It is noted that KBC is imposed on a moving interface at $r = R_0 + R_1$, whose location is not known *a priori*. Therefore, the domain perturbation method is applied to find a boundary condition which is to be imposed on an unperturbed interface. From the Taylor series expansion, we obtain the following expressions which are correct to the first order:

$$\left(\frac{\partial \phi_0}{\partial r} \right)_{r=R_0+R_1} \approx \left(\frac{\partial \phi_0}{\partial r} \right)_{r=R_0} + R_1 \left(\frac{\partial^2 \phi_0}{\partial r^2} \right)_{r=R_0}, \tag{10}$$

$$\left(\frac{\partial \phi_1}{\partial r} \right)_{r=R_0+R_1} \approx \left(\frac{\partial \phi_1}{\partial r} \right)_{r=R_0}. \tag{11}$$

Hence, KBC to be imposed on $r=R_0(t)$, for the zeroth order, is

$$\frac{\partial \phi_0}{\partial r} = \frac{\partial R_0}{\partial t}, \tag{12}$$

and KBC of the first order is, using Eq. (6),

$$\frac{\partial \phi_1}{\partial r} = \frac{\partial R_1}{\partial t} + R_1 \frac{M}{R_0^2}. \tag{13}$$

In addition, combining Eqs. (7) and (12) gives the following expressions for M:

$$M = R_0 \dot{R}_0, \tag{14}$$

and

$$\dot{M} = \dot{R}_0 \dot{R}_0 + \ddot{R}_0 R_0. \tag{15}$$

The dynamic boundary condition (DBC) on a free surface at $r = R_0 + R_1$ is

$$\frac{\partial \phi}{\partial t} + \frac{1}{2} |\nabla \phi|^2 + \frac{\kappa}{\text{We}} = \Delta P_0, \tag{16}$$

where κ denotes the curvature of the interface and ΔP_0 the pressure adjustment. The Weber number, We, is given by $\text{We} = \rho^* U^{*2} R_D^* / \sigma^*$, ρ^* and σ^* being the density and the surface tension of the liquid, respectively. Accurate up to the first order, the curvature κ is expressed as

$$\kappa \approx \frac{1}{R_0} - \frac{1}{R_0^2} \left(R_1 + \frac{\partial^2 R_1}{\partial \theta^2} \right). \tag{17}$$

Domain perturbation is again applied to the DBC to obtain a condition for the unperturbed interface. The DBC to be imposed on $r = R_0(t)$ for the first order is

$$R_1 \left(\frac{\dot{M}}{R_0} - \frac{M^2}{R_0^3} \right) + \frac{\partial \phi_1}{\partial t} + \frac{M}{R_0} \frac{\partial \phi_1}{\partial r} - \frac{1}{\text{We}} \frac{1}{R_0^2} \left(R_1 + \frac{\partial^2 R_1}{\partial \theta^2} \right) = 0. \tag{18}$$

As a solution of the Laplace equation, ϕ_1 is expressed as a superposition of normal modes:

$$\phi_1 = \sum_{m=1}^{\infty} A_m(t) r^m \cos m\theta, \tag{19}$$

where only sinusoidal perturbations are considered. Choosing a potential which corresponds to a disturbance decreasing away from the interface in the inward direction[20] eliminates terms having r^{-m} from the solution of the Laplace equation. Consequently, the shape perturbation is given by

$$R_1 = \sum_{m=1}^{\infty} f_m(t) \cos m\theta. \tag{20}$$

Substitution of Eqs. (19) and (20) into Eq. (13) yields

$$m A_m R_0^{m-1} = \dot{f}_m + \frac{M}{R_0^2} f_m. \tag{21}$$

After substituting Eqs. (19) and (20), Eq. (18) becomes

$$f_m \left[\frac{\dot{M}}{R_0} - \frac{M^2}{R_0^3} + \frac{(m^2-1)}{\mathrm{We}} \frac{1}{R_0} \right] + R_0^m \dot{A}_m + m M R_0^{m-2} A_m = 0. \tag{22}$$

Combining Eqs. (21) and (22), we finally obtain an equation for the shape perturbation amplitude, f_m:

$$\ddot{f}_m + a(t) \dot{f}_m + b(t) f_m = 0, \tag{23}$$

where a and b are given as the following, by virtue of Eqs. (14) and (15):

$$a(t) = 2 \frac{\dot{R}_0}{R_0}, \tag{24}$$

$$b(t) = \frac{(m+1)}{R_0^3} \left[\frac{m(m-1)}{\mathrm{We}} + R_0^2 \ddot{R}_0 \right]. \tag{25}$$

In a special case where R_0 is kept at unity throughout time, the frequency for the mth mode perturbation, ω_m, is given by

$$\omega_m^2 = \left[\frac{m(m^2-1)}{\mathrm{We}} \right]^{1/2}, \tag{26}$$

which is identical to Chandrasekhar's result.[28] See Appendix B for details.

In short, Eq. (23) describes the development of an azimuthal perturbation on a cylindrical spreading sheet. The coefficients are known if the spreading dynamics are known. We note that Eq. (23) is a second order linear ordinary differential equation with variable coefficients. This equation cannot be solved analytically, although stability of the solution can be obtained for limit cases when the coefficients are periodic functions of t.

III. NUMERICAL SIMULATION RESULTS

We begin to investigate the instability by obtaining the base flow solutions. According to the Bowden and Field model,[5] we expect an immediate generation of a liquid jet on impact when the Mach number, $\mathrm{Ma} = U^*/c^*$, U^* being the impact velocity and c^* the sound speed in the liquid medium, is very small. To obtain the base flow solution, i.e., the expansion rate of the liquid jet or contact area, consider the
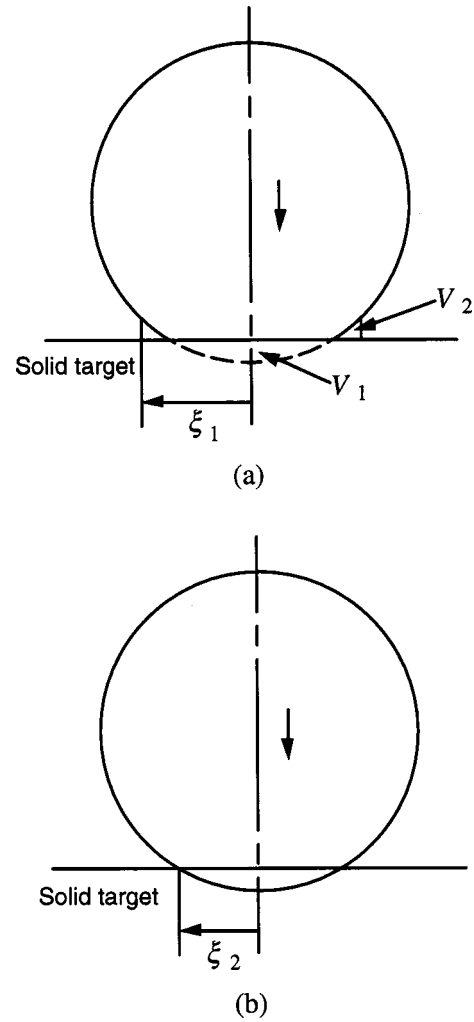

(a)

(b)

FIG. 3. Limiting cases of droplet spreading. The original droplet radius and velocity are both unity after nondimensionalization. (a) Volume V_1 is displaced to V_2 while the droplet descends with the speed of unity. The cylinder radius ξ_1 is expressed as Eq. (27). (b) ξ_2 is the intersection radius of the target surface and the droplet traveling with no deformation.

following simplified case. Suppose that the descending speed of a droplet upon impact is invariant from its original speed, which is often observed in the early stages of spreading.[9,11] As shown in Fig. 3(a), we assume that the bottom of the spherical droplet is displaced to the periphery of the droplet spreading on the surface, resulting in the shape of a truncated-sphere-on-cylinder. Using volume conservation, the radius of the cylinder, or contact radius, is calculated to be

$$\xi_1 = \left[\frac{3}{2} - \frac{9}{8} s^2 - \frac{1}{2} \left(\frac{81}{16} s^4 - \frac{27}{2} s^2 + 12s - 3 \right)^{1/2} \right]^{1/2}, \tag{27}$$

where $s = 1 - t$ ($0 < t < 1/3$). For $t \ll 1$, $\xi_1 \approx 2 t^{1/2}$. It is interesting to note that if the droplet continues to travel after hitting the surface as if the surface did not exist [see Fig. 3(b)], the radius of the intersecting area is expressed as $\xi_2 = (2t - t^2)^{1/2}$, which is approximated to be $\xi_2 \approx (2t)^{1/2}$ for $t \ll 1$. Supposing that the expanding liquid jet exhibits the same tendency as ξ's modeled above upon its generation, we write
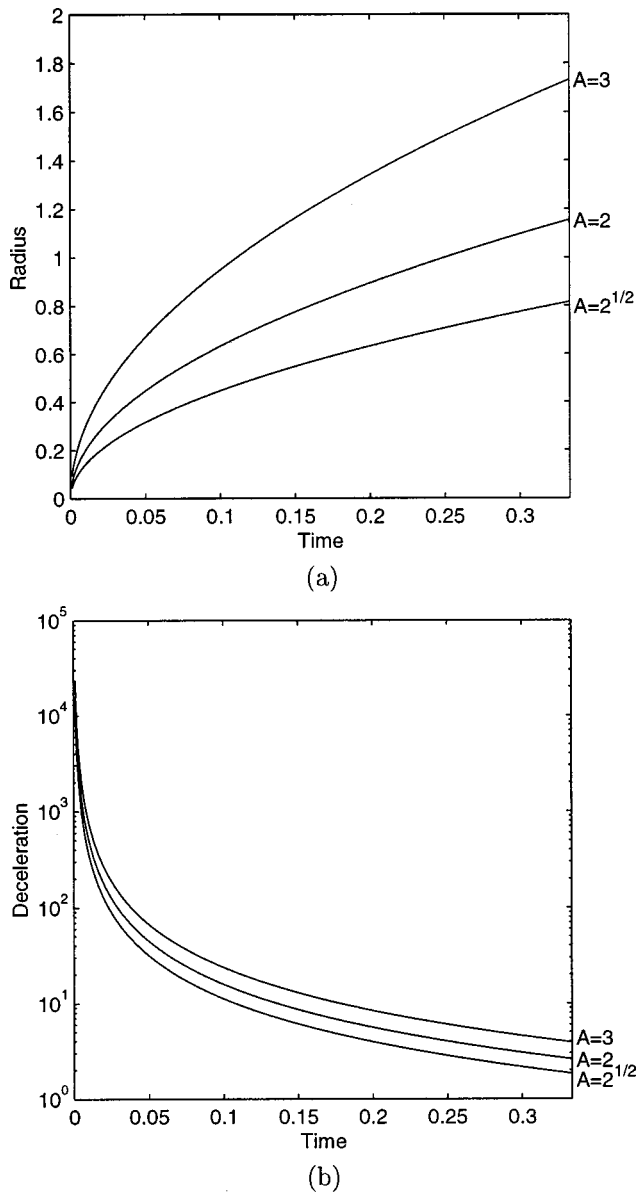
(a)

(b)

FIG. 4. (a) Transient radius profiles of an expanding liquid sheet expressed as $R_0 = At^{1/2}$. (b) Corresponding deceleration. Note that the significant deceleration is experienced by the interface immediately after impact, which drives the Rayleigh–Taylor instability.

$$R_0 = At^{1/2}, \tag{28}$$

where the coefficient A is dependent upon the impact conditions of the droplet. Figure 4 shows the radius and deceleration profiles for the expanding liquid sheet depending on the value of A.
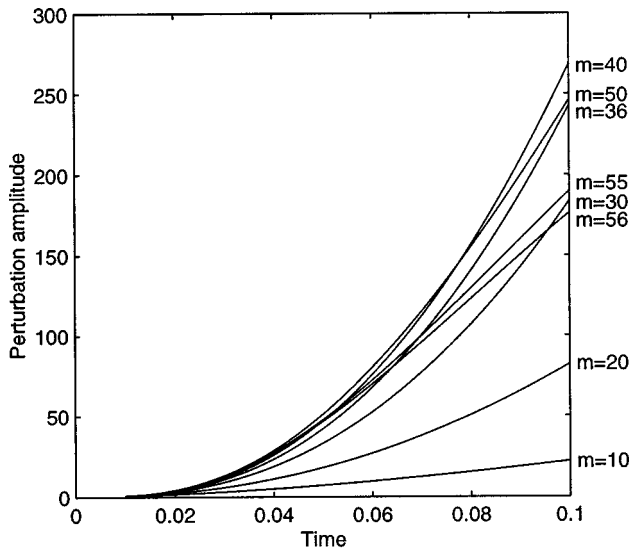
Asymptotic theories of Korobkin and Pukhnachov[29] and a simplified analysis of Oguz and Prosperetti[30] also yield the same time dependence as our limit analysis, providing a theoretical justification of our model. On the other hand, experimental data on the initial stages of droplet impact are hard to find, due to the limitations in the experimental techniques. We recall that the fingers shown in Fig. 1 have already developed when the contact area reaches only a half radius of the original droplet. In many experiments,[6,7,9,31] the radius of the contact area reaches more than that of the original droplet

near $t = 1/3$. The time $t = 1/3$ corresponds, for example, to 500 μs for a droplet with a radius of 3 mm and an impact velocity of 2 m/s. Consequently, it is very difficult to measure the "temporal evolution" of the contact area radius during the very short period from the moment of impact. Most experiments[7,31–36] reported to date present at most 2 data points in the time span of our interest. Other experimental results[6,9,37] presenting at least 3 points in that time range, appear to agree with the time dependence modeled by the theoretical considerations above.
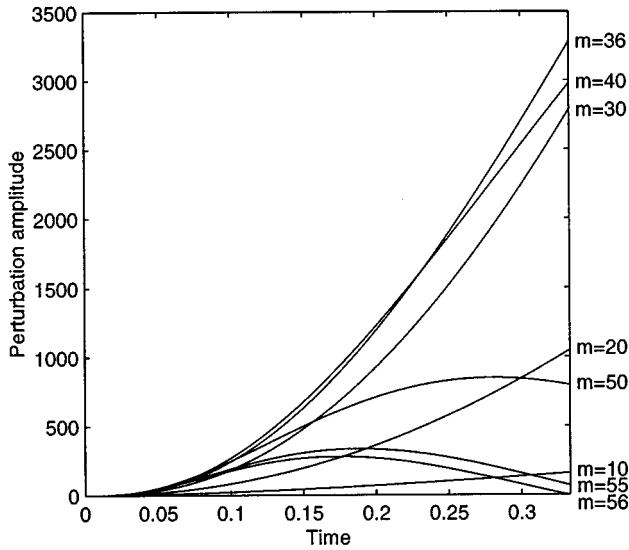
In the context of the Rayleigh–Taylor instability, when the expanding liquid decelerates with respect to a lighter atmospheric gas, the liquid tends to be destabilized while the surface tension has a stabilizing effect. It is possible to approximately predict stability by observing the behavior of the coefficients a and b or by canonical transformation (see Appendix C). However, because of the time-dependent coefficients of Eq. (23), only numerical simulation can exactly predict the wave number of maximum instability and the rate of growth for the shape perturbation. Based on the base solutions, we numerically solve Eq. (23) under given initial conditions such as $f_m = 1$ and $\dot{f}_m = 0$, and $f_m = 0$ and $\dot{f}_m = 1$. The modified Euler method has been employed to solve the initial value problem.[38]

Factors which determine the magnitude of deceleration of a liquid interface, i.e., the driving mechanism of the Rayleigh–Taylor instability, include the coefficient A and the initiation time of perturbation. According to the asymptotic theories,[29] when a perfectly spherical droplet hits the target plane, A is calculated to be $3^{1/2}$ in the present nondimensionalization, which lies between our limiting cases of ξ_1 and ξ_2. In reality, A is supposed to be dependent upon droplet impact conditions as well as the surface curvature of the impacting droplet. Mathematical singularity occurs as $t \to 0$ when both the velocity and the deceleration of the sheet reach infinity. The sheet emerges from a finite initial radius which corresponds to a finite nonzero initiation time. Since it is not clear yet when the liquid sheet emerges, we examine the sensitivity of the perturbation analysis to the perturbation onset time t_i. In the meantime, the effects of impact inertia and surface tension are manifested through the Weber number in our analysis. The presence of surface tension, which stabilizes the interface, leads to the mode of maximum instability. In the following we present the numerical simulation results, including the roles of such parameters as described above.

Figure 5 shows the temporal evolution of shape perturbations for different wave numbers. For a computation time range, we use the limit to which Eq. (27) holds, i.e., $t = 1/3$. Perturbations of different wave numbers compete with one another and the mode number of maximum instability varies with time, unlike time-independent coefficient systems. In addition, neither the growth rate of the perturbation nor the cutoff wave number is easily defined. As predicted in Appendix C, the perturbations of high wave numbers are stabilized as t increases although the instants when the amplitudes alter their slopes do not exactly coincide with those at which the b's change sign. In Fig. 5, the perturbation amplitude of $m = 56$ even decays to a value less than the
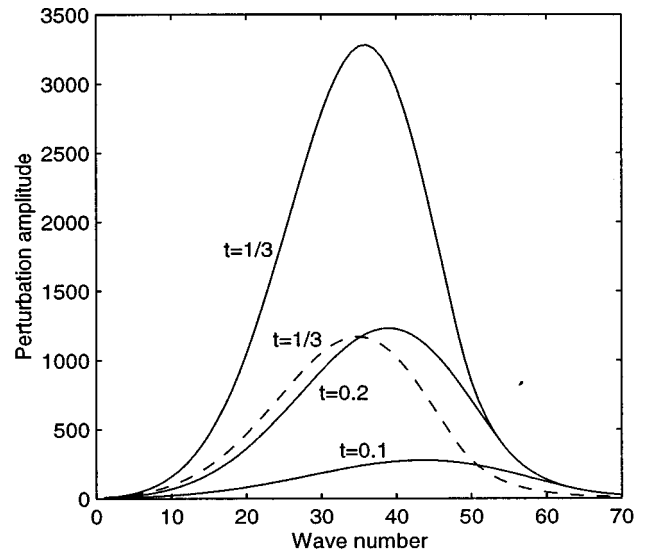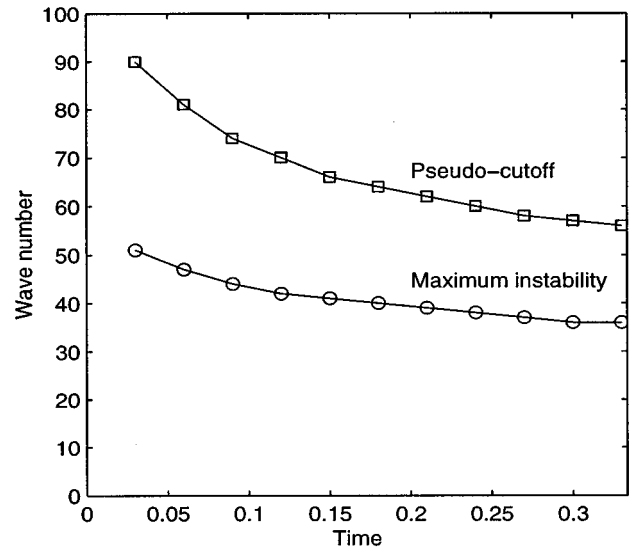
FIG. 5. (a) Temporal evolution of the shape amplitudes of various wave numbers until $t=0.1$. (b) Temporal evolution of the shape amplitudes until $t=1/3$. Initial conditions at $t=t_i$ are $f_m=1$ and $\dot{f}_m=0$. The computation was performed for $R_0=2t^{1/2}$, $t_i=0.01$, and We$=500$. Perturbations of $m=40$ and 50 are exceeded by that of $m=36$ during spreading. Perturbations of $m=50$, 55, and 56 decay after an initially growing period.

FIG. 6. (a) Perturbation amplitude versus wave numbers for different time. Initial conditions for solid lines are $f_m=1$ and $\dot{f}_m=0$. Initial conditions for a dotted line are $f_m=0$ and $\dot{f}_m=100$. The computation was performed for $R_0=2t^{1/2}$, $t_i=0.01$, and We$=500$. (b) Changes of a mode number of maximum instability and a pseudo-cutoff wave number with time. Computation conditions are those of the solid lines in (a).

initially assigned one before t reaches 1/3. We define such a wave number that is less than the so-found wave number by one, as a pseudo-cutoff wave number. In this case, it is 55. Note that our definition of the pseudo-cutoff wave number is different from the criteria used in Appendix C, which are used to judge whether the perturbation amplitudes will grow unboundedly.

Figure 6(a) shows that there exists a wave number which maximizes the amplitude perturbation at every moment during spreading. Furthermore, the number tends to slightly decrease during spreading [Fig. 6(b)], which appears to coincide with an experimentally observed reduction in the number of fingers at the spreading edge.[11] More studies are required to understand how fingers merge during spreading

and which wave number manifests itself in the competition of many modes during spreading. Such questions can be answered by considering the nonlinear effects of finite amplitude perturbations, which are beyond the scope of the present work. Nonetheless, according to our linear theory, high wave numbers excited in the earlier stages of impact are overwhelmed by lower wave numbers in the course of spreading, as deceleration decreases. Figure 7 shows the development of azimuthal disturbances at the modes of maximum instability based on the simulation results. A droplet with a higher Weber number [We$=500$, Fig. 7(b)] develops a much more unstable spreading front than one with a lower Weber number [We$=50$, Fig. 7(a)].

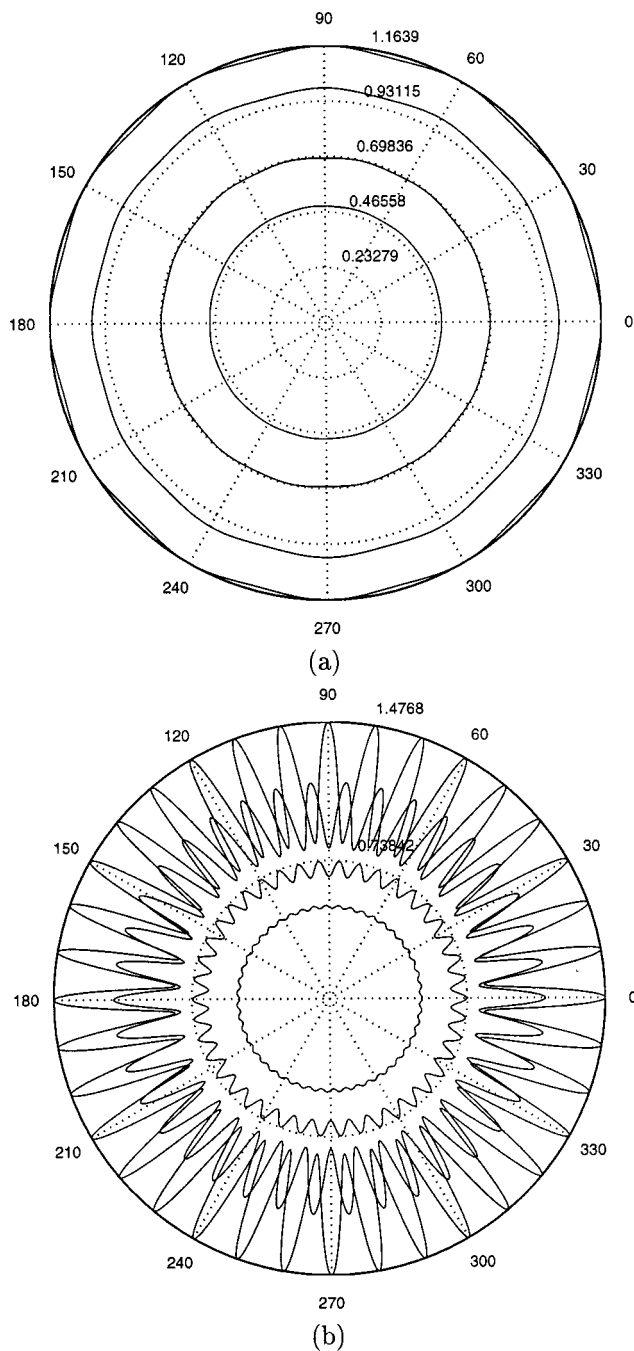Effects of the coefficient A, or the expansion rate of the

(a)

(b)

FIG. 7. Growth of azimuthal disturbances during spreading at the modes of maximum instability. Initial conditions are $f_m = 1 \times 10^{-4}$ and $\dot{f}_m = 0$. The computation was performed for $R_0 = 2t^{1/2}$ and $t_i = 0.01$. (a) Shape evolutions when We=50. From the innermost corrugated circle, $t = 0.06 (m=15)$, $0.12 (m=14)$, $0.24 (m=12)$, $1/3 (m=12)$. (b) Shape evolutions when We =500. From the innermost corrugated circle, $t = 0.06 (m=47)$, $0.12 (m=42)$, $0.24 (m=38)$, $1/3 (m=36)$.

(a)

(b)

FIG. 8. Effect of the coefficient A on instability. The computation was performed for $t_i = 0.01$ and We=500. (a) Wave number of maximum instability versus A. (b) Perturbation amplitude of those numbers versus A.

liquid sheet, on instability are shown in Fig. 8. We note that when the sheet radius is given by Eq. (28), a high expansion rate due to large A results in a high magnitude of deceleration, which eventually promotes the instability of higher wave numbers. Figure 9 illustrates the effect of perturbation onset time on instability. Perturbations initiated earlier exhibit larger deceleration, thus promoting instability of higher wave numbers. However, it is noteworthy that the analysis
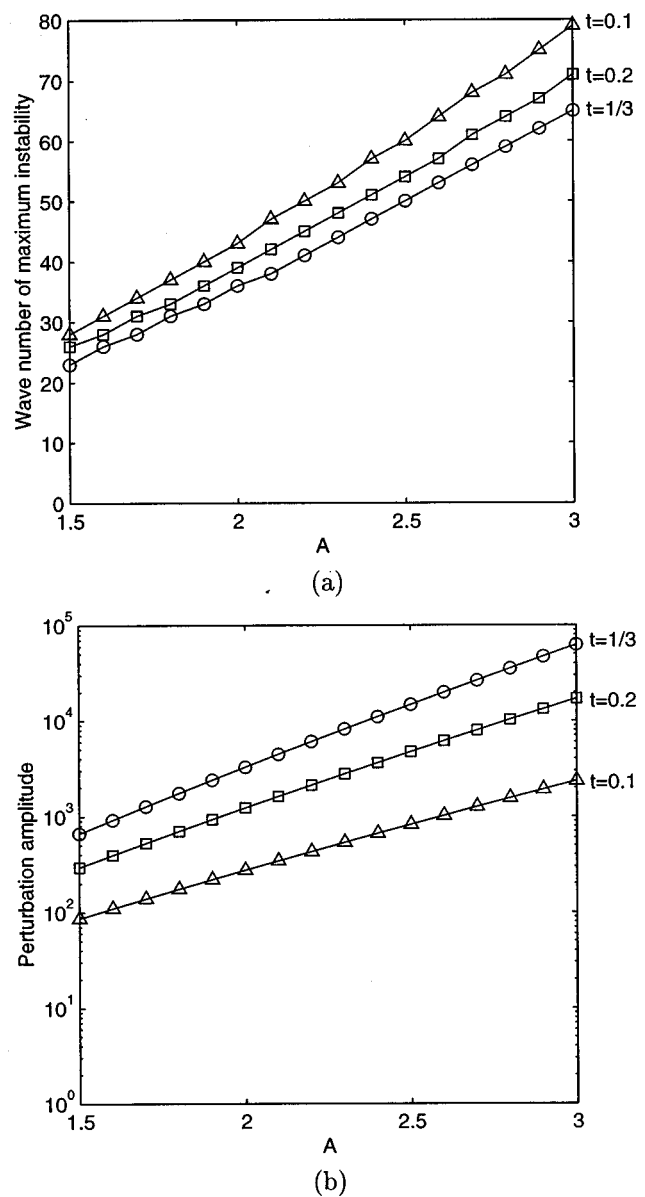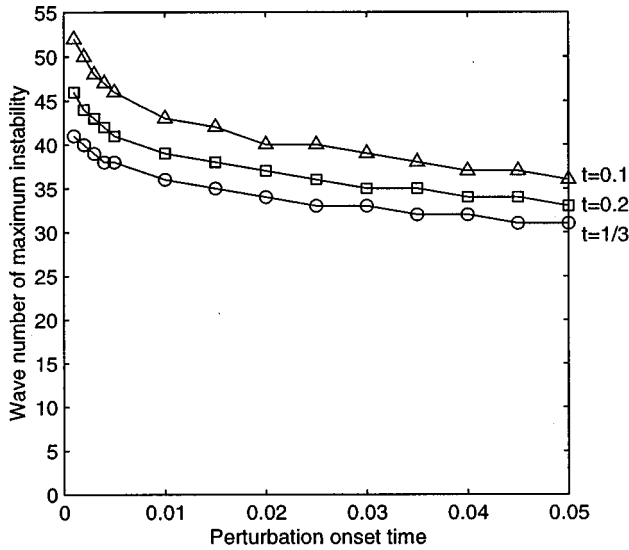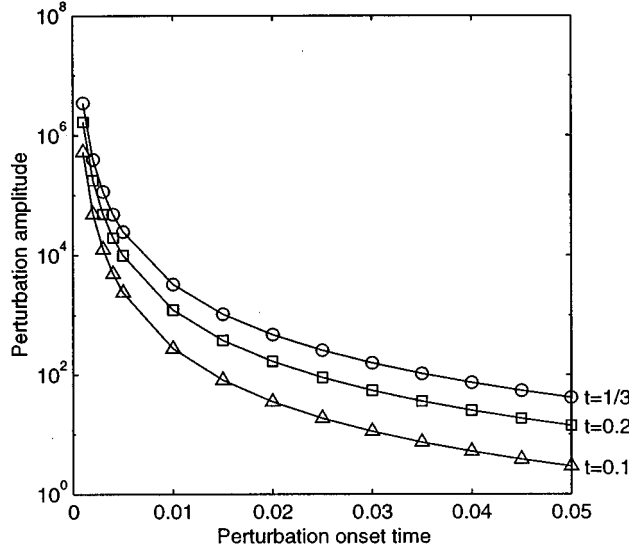
results of the wave number of maximum instability are rather insensitive to t_i. Figure 10 presents the role of the Weber number on the instability. As the Weber number increases, i.e., when the effect of surface tension is weakened and that of inertia is strengthened, a greater number of high modes are excited and perturbation amplitudes increase, as previously illustrated by Fig. 7. This is consistent with the Marmanis and Thoroddsen[12] observation that higher impact speed results in a greater number of fingers.

We compare our numerical results with available experimental data. Thoroddsen and Sakakibara[11] counted the number of fingers of a spreading droplet with We=510 in the present definition of the Weber number, and its spreading diameter versus time was measured as well. According to the spreading diameter measurement, the value of A for the droplet is approximately 2.2 based on the fact that the first
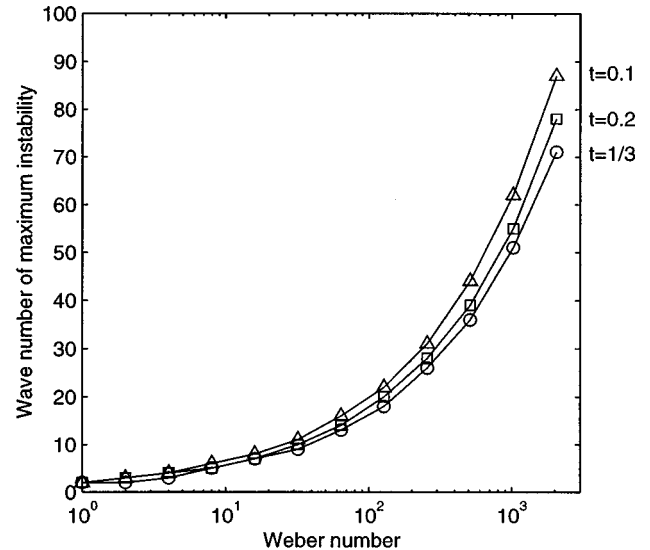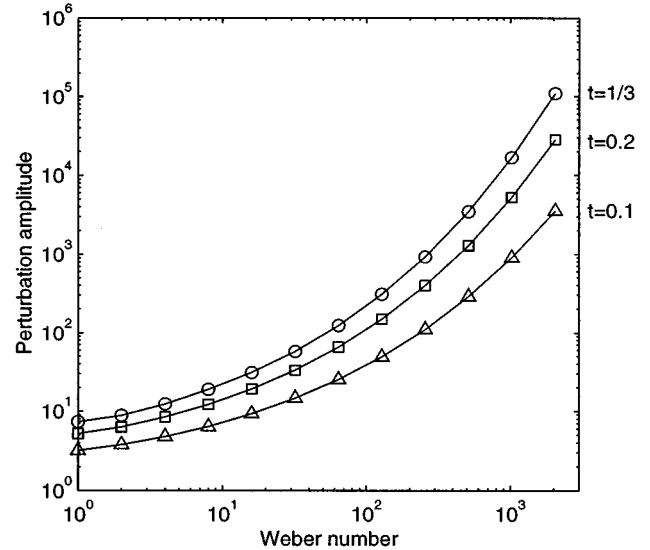
(a)

(b)

FIG. 9. Effect of the perturbation onset time t_i on instability. The computation was performed for $R_0 = 2t^{1/2}$ and We$=500$. (a) Wave number of maximum instability versus t_i. (b) Perturbation amplitude of those numbers versus t_i.

(a)

(b)

FIG. 10. Effect of We on instability. The computation was performed for $R_0 = 2t^{1/2}$ and $t_i = 0.01$. (a) Wave number of maximum instability versus We. (b) Perturbation amplitude of those numbers versus We.

data point of their measurement is located at $R_0 \approx 2$ when $t \approx 0.8$, in the present nondimensionalization. As discussed earlier, A depends on the surface curvature of the impacting droplet which was not maintained as perfectly spherical during the experiments. Our simulation predicts that the wave number of maximum instability for the condition is 63 at the nondimensionalized time $t=0.1$ with $t_i = 5 \times 10^{-4}$. It is recalled that our analysis results are not very sensitive to t_i, e.g., the wave number of maximum instability is 50 at $t = 0.1$ with $t_i = 0.01$. Assuming that the number of fingers initially generated does not change significantly during spreading, as supported by Fig. 1 and Thoroddsen and Sakakibara,[11] the predicted wave numbers are in good agreement with their measured values (Fig. 14 of Thoroddsen and Sakakibara[11]). In addition, we compare our simulation results with the splat shown in Fig. 1, which has approximately

33 fingers. We set $A = 2.2$, based on the available spreading radius measurement in the very early stages of droplet impact with a somewhat similar Weber number—300 (Stow and Hadfield,[9] Fig. 15). Our numerical simulation predicts that the wave number of maximum instability at $t = 0.1$ is 40 with $t_i = 5 \times 10^{-4}$, and 32 with $t_i = 0.01$, which agrees well with the experimental measurement.

IV. CONCLUSIONS

We developed a linear perturbation theory of interface instabilities of a radially-expanding, liquid sheet in cylindrical geometries. The theory was applied to an expanding jet under a spreading droplet as a proposed mechanism of splashing. Our analysis was restricted to the very early stages of droplet impact, i.e., $t < 1/3$. It is because we are interested in studying the fundamental mechanism of the finger forma-

tion rather than the finger evolution. Based on a theoretical model on the contact area expansion in the very early stages of droplet impact, significant deceleration upon the collision triggered the Rayleigh–Taylor instability. The perturbation theory was able to predict the most rapidly growing mode of azimuthal disturbance and its growth rate at each instant during spreading. The mode number of maximum instability changed because of time-dependent coefficients in the amplitude equation. We examined the effects of several parameters on the analysis results, including the transient profile of an interface radius, i.e., the coefficient A, the perturbation onset time t_i, and the Weber number. Experimentally observed number of fingers at the spreading fronts were compared with our predictions, and they agreed well.

It is noted that the parameters examined above, A, t_i, and We, may be interrelated with one another in reality: the impact conditions including the droplet size, velocity, and the surface curvature, not only affect the Weber number, but they also determine the collapsing dynamics of the droplet and its sheet expansion characteristics: A and t_i. In addition, it is known that substrate roughness plays a significant role in splashing.[9] The roughness may affect the values of A and t_i, change the mode of the maximum instability, and destabilize the perturbation for a given wave number. Moreover, as the spreading progresses beyond the very initial stages, the azimuthal perturbation grows and nonlinear interactions between modes such as those reported by Thoroddsen and Sakakibara[11] take place. Although it is possible to extend our analysis to include weakly nonlinear terms, such an effort must be combined with including the viscosity in the analysis since soon after the initial stage, the viscous terms can no longer be ignored. To develop an understanding of these topics, future studies are required.

In conclusion, we propose the Rayleigh–Taylor instability as a mechanism to destabilize the rapidly expanding liquid jet, released upon droplet collision with a solid target. Numerical simulations of the temporal evolution of shape perturbations are able to determine the most rapidly growing wave number and the growth rate of perturbation amplitudes. Our analysis reveals that larger impact inertia associated with a higher We, and thus presumably a higher A, promotes interface instability, and prefers a higher wave number for maximum instability. We relate this instability to the fundamental mechanism behind splashing, or fingering, of impacting droplets which is initiated in the very early stages of impact.

ACKNOWLEDGMENTS

APPENDIX A: NONDIMENSIONAL QUANTITIES

The following gives the definitions of the nondimensional quantities used above. Note that all the asterisked symbols denote dimensional quantities, whereas nonasterisked symbols are the corresponding nondimensional quantities:

$$A_m = \frac{A_m^* R_D^{*(m-1)}}{U^*}, \quad f_m = \frac{f_m^*}{R_D^*}, \quad M = \frac{M^*}{R_D^* U^*},$$

$$r = \frac{r^*}{R_D^*}, \quad R = \frac{R^*}{R_D^*}, \quad R_i = \frac{R_i^*}{R_D^*} \quad (i=0,1),$$

$$\nu_r = \frac{\nu_r^*}{U^*}, \quad \nu_\theta = \frac{\nu_\theta^*}{U^*}, \quad t = \frac{t^*}{\tau^*},$$

$$\Delta P_0 = \frac{\Delta P_0^*}{\rho^* U^{*2}}, \quad \phi = \frac{\phi^*}{R_D^* U^*},$$

$$\phi_i = \frac{\phi_i^*}{R_D^* U^*} \quad (i=0,1),$$

$$\kappa = \kappa^* R_D^*.$$

APPENDIX B: THE OSCILLATION FREQUENCY OF PERTURBATIONS TO A CONSTANT RADIUS LIQUID SHEET

In Chandrasekhar,[28] the frequency for the mth mode azimuthal perturbation on a columnar liquid jet ω_m is given by, in the present nondimensionalization,

$$\omega_m^2 = \frac{1}{R_0^3 \text{We}} \frac{x I_m'(x)}{I_m(x)} (m^2 + x^2 - 1), \tag{B1}$$

where $x = kR_0$, k denoting the wave number in the lengthwise direction, and I_m is the modified Bessel function of the first kind, of order m. We show that for a two-dimensional liquid sheet whose unperturbed radius R_0 is kept unity, Eq. (B1) is reduced to Eq. (26). Using the following identities:[39]

$$I_m'(k) = I_{m+1}(k) + \frac{m}{k} I_m(k), \tag{B2}$$

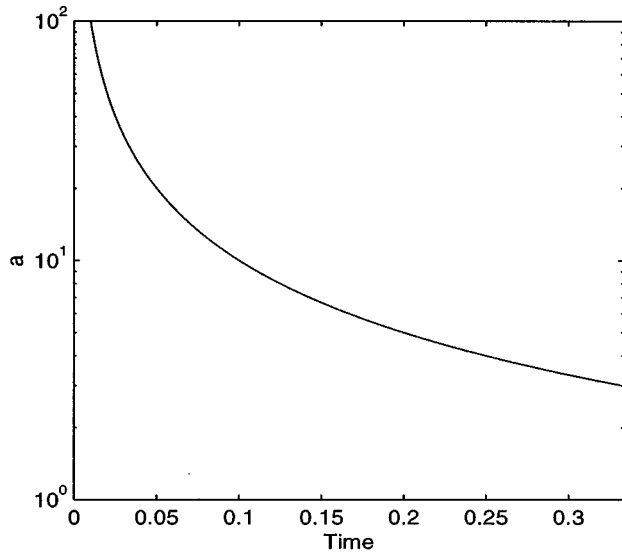$$I_m(k) = \sum_{j=0}^{\infty} \frac{(k/2)^{2j+m}}{j!(j+m)!}, \tag{B3}$$

we find

$$\lim_{k \to 0} \frac{k I_m'(k)}{I_m(k)} = m. \tag{B4}$$
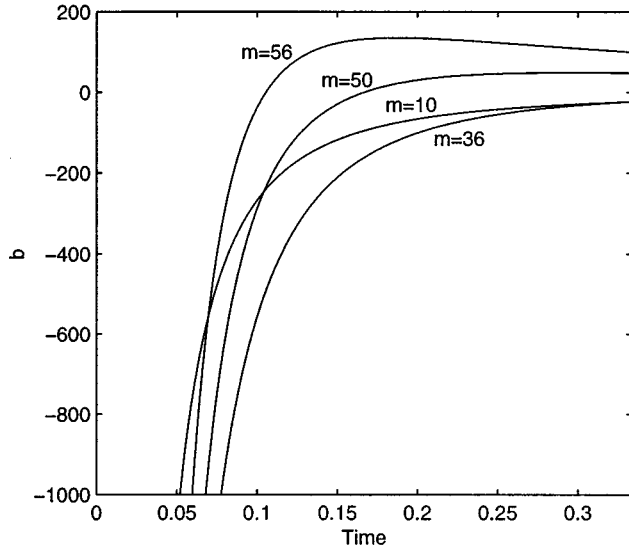
Therefore, in the limit $k \to 0$, Eq. (B1) is identical to Eq. (26).

APPENDIX C: PREDICTIONS OF THE SHAPE STABILITIES

It is possible to predict stability of the equation for the shape perturbation amplitude, Eq. (23), in an approximate manner as the following. First, we approximate the stability by observing the behavior of the coefficients a and b. Figure 11 shows a and b as functions of time, based on Eq. (28). In general, positive a, as shown in Fig. 11(a), corresponds to the positive energy dissipation, thus it has a stabilizing effect. The coefficient, b, the restoring term, is negative at small t for all wave numbers shown in Fig. 11(b), thus it destabilizes the interface. For high wave numbers, b eventually becomes positive during spreading due to the surface

(a)

(b)

FIG. 11. The coefficients of Eq. (23) when $R_0 = 2t^{1/2}$ and We=500. (a) The coefficient a is given by $a = 1/t$. (b) The coefficient b versus time for various wave numbers.

tension, thus it stabilizes the high mode perturbations. The value of m under which b remains negative, denoted as m_1, is calculated to be

$$m_1 = \frac{1}{2}\left[1 + \left(1 + \frac{A^3 \, \text{We}}{t^{1/2}} \right)^{1/2} \right]. \tag{C1}$$

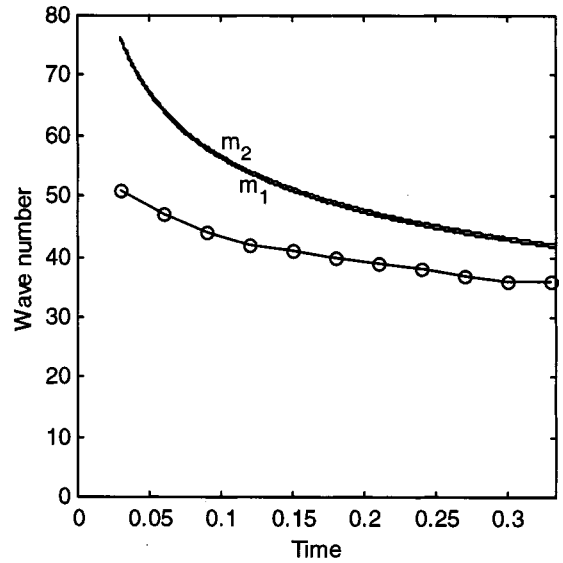Next, we predict the stability by employing the following canonical transformation:

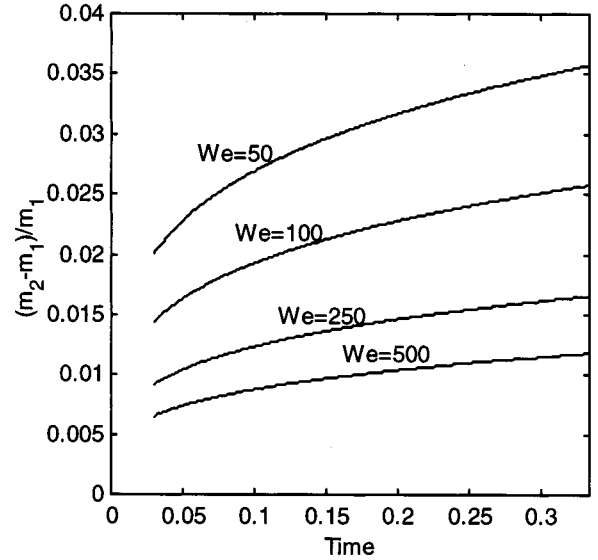$$F_m(t) = g(t) f_m(t), \tag{C2}$$

where the function $g(t)$ is given by

$$g(t) = \exp\left[\frac{1}{2} \int a(t) dt \right]. \tag{C3}$$

We then obtain the transformed equation for $F_m(t)$ as

$$\ddot{F}_m + \beta_m(t) F_m = 0, \tag{C4}$$

(a)

(b)

FIG. 12. (a) The wave numbers m_1 and m_2 versus time. The wave numbers of maximum instability (circles) are from Fig. 6. (b) Normalized differences of m_1 and m_2 versus time at different Weber numbers.

where

$$\beta_m(t) = b - \tfrac{1}{2}\dot{a} - \tfrac{1}{4}a^2. \tag{C5}$$

The quantity $\beta_m(t)$ determines whether $F_m(t)$ is oscillatory or nonoscillatory. Since $f_m = g^{-1}F_m$ and $a(t)$ is positive [Fig. 11(a)], the mode that will grow unboundedly is necessarily a mode for which $\beta_m(t) < 0$. The value of m, under which $\beta_m(t)$ remains negative, denoted as m_2, is calculated to be

$$m_2 = \left(\frac{A^3 \, \text{We}}{4t^{1/2}} + 1 \right)^{1/2}. \tag{C6}$$

Figure 12(a) shows m_1 and m_2 versus time during expansion of the liquid sheet when $A=2$ and We=500. The

wave numbers of maximum instability are also shown for comparison. The values of m_1 and m_2 appear to be almost identical. The normalized differences of m_1 and m_2 are shown in Fig. 12(b). They are indeed fairly close for different Weber numbers.

[1] A. M. Worthington, ''On the forms assumed by drops of liquid falling on a horizontal plate,'' Proc. R. Soc. London **25**, 261 (1877).

[2] A. M. Worthington, ''A second paper on the forms assumed by drops of liquid falling on a horizontal plate,'' Proc. R. Soc. London **25**, 498 (1877).

[3] O. G. Engel, ''Waterdrop collisions with solid surfaces,'' J. Res. Natl. Bur. Stand. **54**, 281 (1995).

[4] F. H. Harlow and J. P. Shannon, ''The splash of a liquid drop,'' J. Appl. Phys. **38**, 3855 (1967).

[5] F. P. Bowden and J. E. Field, ''The brittle fracture of solids by liquid impact, by solid impact, and by shock,'' Proc. R. Soc. London, Ser. A **282**, 331 (1964).

[6] S. Chandra and C. T. Avedisian, ''On the collision of a droplet with a solid surface,'' Proc. R. Soc. London, Ser. A **432**, 13 (1991).

[7] J. Fukai, Y. Shilba, T. Yamamoto, O. Miyatake, D. Poulikakos, C. M. Megaridis, and Z. Zhao, ''Wetting effects on the spreading of a liquid droplet colliding with a flat surface: Experiment and modeling,'' Phys. Fluids **7**, 236 (1995).

[8] Z. Levin and P. V. Hobbs, ''Splashing of water drops on solid and wetted surfaces: hydrodynamic and charge separation,'' Philos. Trans. R. Soc. London, Ser. A **269**, 555 (1971).

[9] C. D. Stow and M. G. Hadfield, ''An experimental investigation of fluid flow resulting from the impact of a water drop with an unyielding dry surface,'' Proc. R. Soc. London, Ser. A **373**, 419 (1981).

[10] CHR. Mundo, M. Sommerfield, and C. Tropea, ''Droplet-wall collisions: experimental studies of the deformation and breakup process,'' Int. J. Multiphase Flow **21**, 151 (1995).

[11] S. T. Thoroddsen and J. Sakakibara, ''Evolution of the fingering pattern of an impacting drop,'' Phys. Fluids **10**, 1359 (1998).

[12] H. Marmanis and S. T. Thoroddsen, ''Scaling of the fingering pattern of an impacting drop,'' Phys. Fluids **8**, 1344 (1996).

[13] R. F. Allen, ''The role of surface tension in splashing,'' J. Colloid Interface Sci. **51**, 350 (1975).

[14] M. B. Lesser, ''Analytical solutions of liquid-drop impact problems,'' Proc. R. Soc. London, Ser. A **377**, 289 (1981).

[15] A. A. Korobkin, ''Asymptotic theory of liquid–solid impact,'' Philos. Trans. R. Soc. London, Ser. A **355**, 507 (1997).

[16] G. I. Taylor, ''The instability of liquid surfaces when accelerated in a direction perpendicular to their planes. I,'' Proc. R. Soc. London, Ser. A **201**, 192 (1950).

[17] R. Menikoff, R. C. Mjolsness, D. H. Sharp, C. Zemach, and B. J. Doyle, ''Initial value problem for Rayleigh–Taylor instability of viscous fluids,'' Phys. Fluids **21**, 1674 (1978).

[18] G. Tryggvason, ''Numerical simulations of the Rayleigh–Taylor instability,'' J. Comput. Phys. **75**, 253 (1988).

[19] M. Berning and A. M. Rubenchik, ''A weakly nonlinear theory for the dynamical Rayleigh–Taylor instability,'' Phys. Fluids **10**, 1564 (1998).

[20] M. S. Plesset, ''On the stability of fluid flows with spherical symmetry,'' J. Appl. Phys. **25**, 96 (1954).

[21] M. S. Plesset and T. P. Mitchell, ''On the stability of the spherical shape of a vapor cavity in a liquid,'' Q. Appl. Math. **13**, 419 (1956).

[22] G. Birkhoff, ''Stability of spherical bubbles,'' Q. Appl. Math. **13**, 451 (1956).

[23] G. R. Baker, D. I. Meiron, and S. A. Orszag, ''Boundary integral methods for axisymmetric and three-dimensional Rayleigh–Taylor instability problems,'' Physica D **12**, 19 (1984).

[24] S. Hilgenfeldt, M. P. Brenner, S. Grossmann, and D. Lohse, ''Analysis of Rayleigh–Plesset dynamics for sonoluminescing bubbles,'' J. Fluid Mech. **365**, 171 (1998).

[25] M. S. Plesset and A. Prosperetti, ''Bubble dynamics and cavitation,'' Annu. Rev. Fluid Mech. **9**, 145 (1977).

[26] Z. C. Feng and L. G. Leal, ''Nonlinear bubble dynamics,'' Annu. Rev. Fluid Mech. **29**, 201 (1997).

[27] M. P. Brenner, D. Lohse, and T. F. Dupont, ''Bubble shape oscillations and the onset of sonoluminescence,'' Phys. Rev. Lett. **75**, 954 (1995).

[28] S. Chandrasekhar, *Hydrodynamic and Hydromagnetic Stability* (Oxford University Press, Oxford, 1961), p. 538.

[29] A. A. Korobkin and V. V. Pukhnachov, ''Initial stage of water impact,'' Annu. Rev. Fluid Mech. **20**, 159 (1988).

[30] H. N. Oguz and A. Prosperetti, ''Surface-tension effects in the contact of liquid surfaces,'' J. Fluid Mech. **203**, 149 (1989).

[31] M. Pasandideh-Fard, Y. M. Qiao, S. Chandra, and J. Mostaghimi, ''Capillary effects during droplet impact on a solid surface,'' Phys. Fluids **8**, 650 (1996).

[32] L. H. J. Wachters and N. A. J. Westerling, ''The heat transfer from a hot wall to impinging water drops in the spheroidal state,'' Chem. Eng. Sci. **21**, 1047 (1966).

[33] L. Cheng, ''Dynamic spreading of drops impacting onto a solid surface,'' Ind. Eng. Chem. Process Des. Dev. **16**, 192 (1977).

[34] M. Kurokawa and S. Toda, ''Heat transfer of an impacted single droplet on the wall,'' ASME/JSME Thermal Eng. Proc. **2**, 141 (1991).

[35] G. Trapaga, E. F. Matthys, J. J. Valencia, and J. Szekely, ''Fluid flow, heat transfer, and solidification of molten metal droplets impinging on substrates: Comparison of numerical and experimental results,'' Metall. Mater. Trans. B **23B**, 701 (1992).

[36] M. Pasandideh-Fard, R. Bhola, S. Chandra, and J. Mostaghimi, ''Deposition of tin droplets on a steel plate: simulations and experiments,'' Int. J. Heat Mass Transf. **41**, 2929 (1998).

[37] S. Chandra and C. T. Avedisian, ''Observation of droplet impingement on a ceramic porous surface,'' Int. J. Heat Mass Transf. **35**, 2377 (1992).

[38] S. Nakamura, *Applied Numerical Methods with Software* (Prentice–Hall, Englewood Cliffs, NJ, 1991), p. 295.

[39] F. B. Hildebrand, *Advanced Calculus for Applications*, 2nd ed. (Prentice–Hall, Englewood Cliffs, NJ, 1976), pp. 147–149.